Surface and interfacial waves in a strongly stratified upper ocean

Johannes Gemmrich and Adam Monahan

2021

Original citation:
Gemmrich, J., & Monahan, A. (2020). Surface and interfacial waves in a strongly stratified upper ocean. *Journal of Physical Oceanography*, *51*(2), 269–278. https://doi.org/10.1175/jpo-d-20-0073.1

Surface and Interfacial Waves in a Strongly Stratified Upper Ocean

JOHANNES GEMMRICH[a] AND ADAM MONAHAN[b]

[a] *Department of Physics and Astronomy, University of Victoria, Victoria, British Columbia, Canada*
[b] *School of Earth and Ocean Sciences, University of Victoria, Victoria, British Columbia, Canada*

(Manuscript received 31 March 2020, in final form 29 September 2020)

ABSTRACT: In an idealized two-layer fluid, surface waves can generate waves at the internal interface through class-3 resonant triads in which all waves are propagating in the same direction. The triads are restricted to wavenumbers above a critical value k_{crit} that depends on the density ratio R between the two layers and their depths. We perform numerical simulations to analyze the evolution of a surface wave field, initially specified by a Pierson–Moskowitz-type spectrum, for $R = 0.97$ (representing a realistic lower a bound for oceanic stratification). At high initial steepness and peak wavenumber $k_p \ll k_{crit}$, the energy increases in the spectral tail; as a parameterization of resulting wave breaking, at each time step individual waves with a steepness greater than the limiting Stokes steepness are removed. The energy change of the surface wave field is a combination of energy transfer to the interfacial waves, spectral downshift, and wave breaking dissipation. At wavenumbers $\gtrsim 0.6k_p$ there is a net loss of energy, with the greatest dissipation at $\approx 1.3k_p$. The maximum gain occurs at $\approx 0.5k_p$. The onset of the spectral change shows a strong threshold behavior with respect to the initial wave steepness. For steep initial waves the integrated energy dissipation can reach >30% of the initial energy, and only ≈1% of the initial surface wave energy is transferred to the interfacial wave field. The spectral change could be expressed as an additional dissipation source term, and coupled ocean–wave models should include additional mixing associated with the interfacial waves and enhanced wave breaking turbulence.

KEYWORDS: Internal waves; Wave breaking; Waves, oceanic; Atmosphere-ocean interaction; Sea state; Surface layer

1. Introduction

Surface waves on oceans and lakes play an important role in many aspects of physical oceanography, ocean engineering, and climate science. Waves enhance the air–water exchange processes of momentum, gases, and heat; generate turbulence in the near-surface layer; can pose risks to marine operations and structures; and are a source of renewable energy. Spectral wave models like Wavewatch III (WAVEWATCH III Development Group 2016) or WAM routinely predict properties of surface waves with high accuracy in the open ocean and somewhat lower skill in coastal or enclosed waters (Cavaleri et al. 2018). In these models the water column is assumed to have uniform density. However, in some situations a shallow, well-mixed surface layer of less dense water exists, and waves are propagating on a two-layer fluid. Such conditions occur for example in estuaries where freshwater river outflow overlies the salty oceanic water, or polar regions where ice melt can generate a surface layer of warm less saline water.

Here we analyze how the evolution of the surface wave field in a two-layer situation differs from that using the standard assumption of a homogeneous fluid. The density difference at the bottom of the surface layer can support internal waves. If the lower layer is density-stratified the wind-generated surface waves are known to generate internal gravity waves; however, their generation has little feedback on the surface wave field (Thorpe 1966; Olbers and Eden 2016). In the case of a homogeneous lower layer, in contrast, the generated waves are trapped at the interface. Generation of such interfacial waves will require energy. A well-known example is the ''dead water'' phenomenon of fjords that is known to slow down small vessels (Ekman 1904). Similarly, if the interfacial waves are excited by surface waves, it is likely that this process will affect the energetics of the surface wave field. Ball (1964) established two classes of resonant triad interactions between surface waves and interfacial waves, where two oppositely propagating surface (interfacial) waves are in resonance with an interfacial (surface) wave. Ma (1983) analyzed resonant interactions of surface waves and internal waves propagating in the same direction but restricted to the special case where the group speed of the surface wave envelope matches the phase speed of the interfacial wave.

The necessary conditions for the triad interactions mentioned above are very restrictive and therefore these triad interactions do likely not affect the surface wave field in the ocean. Such an influence may, however, exist for a recently discovered class-3 triad interaction between two surface waves and one interfacial wave, all propagating in the same direction, and occurring through a wide range of wavenumbers found in typical ocean wave spectra (Alam 2012). The wavenumber of the interfacial wave is much smaller than those of the surface waves, and near-resonant interactions spread the energy further to lower and higher harmonics of the initial waves. These properties suggest that class-3 triads could be a relevant process in the evolution of the surface wave field.

Class-3 triads are restricted to surface wavenumbers greater than a critical wavenumber k_{crit}, which depends on the density ratio and the depth ratio of the two layers. For density ratios higher than those characteristic for ocean conditions, Tanaka and Wakayama (2015) studied the evolution of the energy

Corresponding author: Johannes Gemmrich, gemmrich@uvic.ca

DOI: 10.1175/JPO-D-20-0073.1

spectra of the prescribed surface waves $S_s(k)$ and the emerging interfacial waves $S_i(k)$ based on class-3 triads. They found a gradual downshift of the spectral peak of the surface waves that halts at k_{crit}, where a sharp peak in $S_s(k)$ forms. Such a profound change in the spectral shape would significantly affect other wave processes like the energy input from the wind to the waves, the energy dissipation due to wave breaking (Banner et al. 2002) and the occurrence rate of unexpected waves (Gemmrich and Garrett 2008) and rogue waves (Dysthe et al. 2008; Gemmrich and Garrett 2011). Here we extend the work by Tanaka and Wakayama (2015) to ocean conditions that can be approximated by a two-layer fluid with a significant density difference characteristic for estuarine and high-latitude settings, but much stronger than found in the case of a typical open ocean surface mixed layer.

2. Model description

We consider waves propagating on a shallow homogeneous upper layer, denoted by subscript u, overlaying a homogeneous, much thicker lower layer, denoted by subscript l, with mean thickness h_u, h_l, small deviations of the layer thickness η_u, η_l, and densities ρ_u, ρ_l, respectively. Waves are propagating in the positive x direction, and the vertical coordinate z is positive upward. Following Alam (2012) we assume irrotational motion in both layers, specified by the velocity potential $\Phi_u(x, z, t)$ and $\Phi_l(x, z, t)$. The motion in the two layers is governed by the following set of equations (Alam 2012):

$$\nabla^2\Phi_u = 0, \quad -h_u + \eta_l < z < \eta_u, \tag{1a}$$

$$\nabla^2\Phi_l = 0, \quad -h_u - h_l < z < -h_u + \eta_l, \tag{1b}$$

$$\frac{\partial\eta_u}{\partial t} + \frac{\partial\eta_u}{\partial x}\frac{\partial\Phi_u}{\partial x} - \frac{\partial\Phi_u}{\partial z} = 0, \quad z = \eta_u, \tag{1c}$$

$$\frac{\partial\Phi_u}{\partial t} + \frac{1}{2}\left[\left(\frac{\partial\Phi_u}{\partial x}\right)^2 + \left(\frac{\partial\Phi_u}{\partial z}\right)^2\right] + g\eta_u = 0, \quad z = \eta_u, \tag{1d}$$

$$\frac{\partial\eta_l}{\partial t} + \frac{\partial\eta_l}{\partial x}\frac{\partial\Phi_u}{\partial x} - \frac{\partial\Phi_u}{\partial z} = 0, \quad z = -h_u + \eta_l, \tag{1e}$$

$$\frac{\partial\eta_l}{\partial t} + \frac{\partial\eta_l}{\partial x}\frac{\partial\Phi_l}{\partial x} - \frac{\partial\Phi_l}{\partial z} = 0, \quad z = -h_u + \eta_l, \tag{1f}$$

$$\rho_u\left\{\frac{\partial\Phi_u}{\partial t} + \frac{1}{2}\left[\left(\frac{\partial\Phi_u}{\partial x}\right)^2 + \left(\frac{\partial\Phi_u}{\partial z}\right)^2\right] + g\eta_l\right\} - \rho_l\left\{\frac{\partial\Phi_l}{\partial t} + \frac{1}{2}\left[\left(\frac{\partial\Phi_l}{\partial x}\right)^2 + \left(\frac{\partial\Phi_l}{\partial z}\right)^2\right] + g\eta_l\right\} = 0, \quad z = -h_u + \eta_l, \tag{1g}$$

$$\frac{\partial\Phi_l}{\partial z} = 0, \quad z = -h_u - h_l, \tag{1h}$$

where g is the acceleration due to gravity. The elevations of the surface and the interface are taken to be superpositions of a large number of small-amplitude plane waves:

$$\eta_u = a_s e^{i(k_s x - \omega_s t)} \quad \text{and} \quad \eta_l = a_i e^{i(k_i x - \omega_i t)}, \tag{2}$$

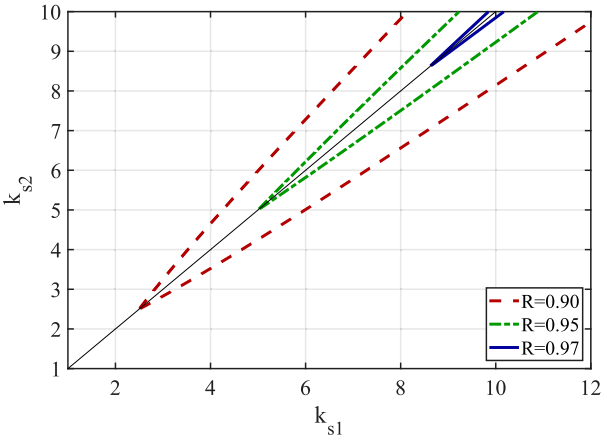

FIG. 1. Conditions on surface wave wavenumbers k_{s1} and k_{s2} to form three-wave resonant interactions, as a function of the density ratio R. Wave numbers are normalized by the thickness of the surface layer h_u and the thickness of the lower layer is $h_l = 100h_u$.

where a_s, ω_s, k_s and a_i, ω_i, k_i are the amplitude, frequency, and wavenumbers of the individual surface waves and interfacial waves, respectively, and a_s, a_i evolve in time. At the free surface the kinematic and dynamic boundary conditions are given by Eqs. (1c) and (1d), respectively. At the interface the kinematic boundary conditions are (1e) and (1f), and the dynamic boundary condition is (1g). Equation (1h) specifies that there is no vertical motion at the (flat) bottom. The linear dispersion relation (Lamb 1932, Article 231)

$$\omega^4[\coth(kh_u)\coth(kh_l) + R] - \omega^2[\coth(kh_u) + \coth(kh_l)]gk + (1 - R)g^2k^2 = 0, \tag{3}$$

with density ratio $R = \rho_u/\rho_l$, is quadratic in ω^2 and has two solutions, ω_s^2, ω_i^2, for a given wavenumber k. The characteristics of the waves depend strongly on R as well as the relative layer thickness. For example, for wavelengths short compared to the layer thickness, i.e., $kh_{u,l} \gg 1$, Eq. (3) leads to following two approximations:

$$\omega_i^2 = \frac{1 - R}{1 + R}gk \tag{4}$$

for the interfacial wave, and the deep-water dispersion relation

$$\omega_s^2 = gk \tag{5}$$

for the surface wave.

Contrary to gravity waves on homogeneous deep water, where a minimum of four free waves are required to form resonance (Phillips 1960), the dispersion relation (3) allows for resonance of three waves (Alam 2012):

$$k_{s2} = k_{s1} \pm k_i, \quad \omega_{s2} = \omega_{s1} \pm \omega_i, \tag{6}$$

where two surface waves with wavenumbers k_{s1}, k_{s2} and frequencies ω_{s1}, ω_{s2} transfer energy to an interfacial wave with wavenumber k_i and frequency ω_i. Exact resonance occurs for k_{s1}, k_{s2} restricted to the resonance curve, which is a function of the density ratio R and the layer depths h_u, h_l (Fig. 1).

Triads are only possible for surface wavenumbers greater than a critical wavenumber k_{crit}, and for increasing density ratios triads become more severely restricted to high wavenumbers. Class-3 triads can also develop between two interfacial waves and one surface waves, all propagating in the same directions. However, as stated in Alam (2012) they are only possible "for very strong density ratios, atypical of real oceans," and therefore are not considered here.

The set of Eqs. (1) can be solved using the high-order spectral method (HOS) (Dommermuth and Yue 1987) described in detail in Alam et al. (2009). For this, Eqs. (1) are expanded to evolution equations for the surface and interfacial elevations, η_u and η_l, and the velocity potentials at the free surface $\Phi_u^S(x, t) = \Phi_u(x, \eta_u, t)$ and at the interface $\Psi^I(x, t) = \Phi_u(x, -h_u + \eta_l, t) - R\Phi_l(x, -h_u + \eta_l, t)$:

$$\frac{\partial \eta_u}{\partial t} = -\frac{\partial \eta_u}{\partial x}\frac{\partial \Phi_u^S}{\partial x} + \left[1 + \left(\frac{\partial \eta_u}{\partial x}\right)^2\right]\frac{\partial \Phi_u}{\partial z}, \quad z = \eta_u, \tag{7a}$$

$$\frac{\partial \Phi_u^S}{\partial t} = -\frac{1}{2}\left\{\left(\frac{\partial \Phi_u^S}{\partial x}\right)^2 - \left[1 + \left(\frac{\partial \eta_u}{\partial x}\right)^2\right]\left(\frac{\partial \Phi_u}{\partial z}\right)^2\right\} - g\eta_u, \quad z = \eta_u, \tag{7b}$$

$$\frac{\partial \eta_l}{\partial t} = -\frac{\partial \eta_l}{\partial x}\frac{\partial \Phi_u^I}{\partial x} + \left[1 + \left(\frac{\partial \eta_l}{\partial x}\right)^2\right]\frac{\partial \Phi_u}{\partial z}, \quad z = -h_u + \eta_l, \tag{7c}$$

$$\begin{aligned}\frac{\partial \Psi^I}{\partial t} = {} & \frac{1}{2}\left[R\left(\frac{\partial \Phi_u^I}{\partial x}\right)^2 - \left(\frac{\partial \Phi_l^I}{\partial z}\right)^2\right] \\ & + \frac{1}{2}\left[1 + \left(\frac{\partial \eta_l}{\partial x}\right)^2\right]\left[\left(\frac{\partial \Phi_l}{\partial z}\right)^2 - R\left(\frac{\partial \Phi_u}{\partial z}\right)^2\right] \\ & - g\eta_l(1 - R), \qquad z = -h_u + \eta_l.\end{aligned} \tag{7d}$$

The velocity potentials are expanded in perturbation series up to order M in the wave steepness ε:

$$\Phi_u = \sum_{m=1}^{M} \Phi_u^{(m)}(x, z, t), \quad \Phi_l = \sum_{m=1}^{M} \Phi_l^{(m)}(x, z, t), \tag{8}$$

where $()^m$ implies a quantity of order $O(\varepsilon^m)$.

The potentials required at the free surface, $z = \eta_u(x, t)$, and at the interface, $z = -h_u + \eta_l(x, t)$, can be obtained from Taylor series evaluated at the mean, undisturbed surfaces, $z = 0$ and $z = -h_u$. The single boundary conditions at the time- and space-varying surface and interface have been transformed into a series of linearized boundary conditions for the perturbed potentials $\Phi_u^{(m)}$ and $\Phi_l^{(m)}$, $m = 1, \ldots, M$, at fixed vertical locations, which can be solved sequentially, starting from $m = 1$. This way, all terms on the right-hand side of Eqs. (7) can be obtained. The integration of (7) with respect to t is performed by the fourth-order Runge–Kutta scheme, yielding the time-varying surface and interfacial elevations and their velocity potentials at all locations x. At second order in the perturbation expansion ($M = 2$) leading-order resonance may occur between a triplet of waves, whereas the four-wave interactions known to occur for waves on a homogeneous fluid require the perturbation to included third-order terms ($M = 3$) (Phillips 1960). Here, the expansion is restricted to $M = 2$.

a. Wave-breaking

As pointed out by Dommermuth and Yue (1987), the expansion of Φ_u around $z = 0$ places an upper limit on the steepness of the free surface, above which the method becomes numerically unstable. In particular they found the energy of steep high wavenumber waves to increase rapidly, and suggested imposing a low-pass filter on the surface elevation record after each time step. However, in a two-layer fluid with $R = 0.97$ the spectral modifications associated with the triad interactions occur predominately at high wavenumbers and a low-pass filter would also remove the effects of these triad interactions. Alternatively, we introduce a physically more intuitive "wave-breaking scheme" that removes individual waves based on their steepness, rather than removing energy solely based on wavenumber.

Energy transfer at high wavenumbers results in increased wave steepness which in turn amplifies the energy transfer in the next time step. Such an accumulation of energy at high wavenumbers results in steep waves. At the end of each time step the surface elevation $\eta_u(x)$ is adjusted by following wave-breaking scheme: The surface elevation $\eta_u(x)$ is copied to a temporary record $\tilde{\eta}_u(x)$, from which short waves riding on longer waves are removed (Banner et al. 2002) and all remaining individual wave crests are identified with the MATLAB toolbox WAFO (Brodtkorb et al. 2000). For each individual wave $k = 1, \ldots, N_W$ we calculate a characteristic wave steepness H_k/λ_k, where N_W is the total number of crests, H_k is the trough-to-crest height of the kth wave, and λ_k the kth distance between two consecutive zero-down crossings of the surface elevation $\tilde{\eta}_u(x)$ without riding waves. Wave crests with a steepness greater than a given threshold are identified and in the original record $\eta_u(x)$ the surface elevation between zero-down crossings associated with these steep waves is multiplied by a factor $\alpha_{bw} < 1$. As the breaking threshold we choose the limiting steepness of a Stokes wave, $H/\lambda = 0.14$ (Stokes 1880), and α_{bw} is taken to be the ratio between the median wave steepness of all waves and the individual wave steepness. This adjustment of the surface elevation also affects the velocity field, and the velocity potential $\Phi_u(x)$ for the affected sections is also scaled by α_{bw}. This ensures the equipartition of potential and kinetic energy remains valid.

We also tested less severe breaking schemes where the steep crests are only reduced to a height slightly below the steepness threshold. This increases the necessary computations, since the wave is likely subject to breaking after the next time step, but we find at long time periods the differences in the spectral evolution are insignificant.

b. Wave field evolution

Similar to Tanaka and Wakayama (2015), we use the HOS scheme to evaluate the evolution of the surface and interface wave spectra in a two-layer fluid, but explore a parameter range that is more applicable to ocean conditions. The model is nondimensionalized with length scale $L = \tilde{h}_u$, mass scale $M = \tilde{\rho}_l \tilde{h}_u^3$, and time scale $T = (\tilde{h}_u/\tilde{g})^{1/2}$, where $\tilde{h}_u$, $\tilde{\rho}_l$, $\tilde{g}$ are dimensional mean upper-layer depth, lower-layer density, and acceleration due to gravity, respectively. All numerical simulations

are based on the nondimensional model and in the following only nondimensional values are presented, unless explicitly stated otherwise.

The HOS simulations of (7) are efficiently performed by a pseudospectral approach, where the spatial derivatives of the velocity potentials are performed in Fourier space, nonlinear terms and products in (7) are calculated in physical space at fixed locations x_j, $j = 1, \ldots, N_x$, and the evolution of the wave field is then calculated at each time step Δt. Details are given in Alam et al. (2009). Our numerical scheme is identical to that of Tanaka and Wakayama (2015), except that we converted it from the original FORTRAN code to MATLAB. We use $N_x = 2^{18}$ evenly spaced points, which allows for $N_k = (2N_x/3) - 2 = 174\,760$ independent wavenumbers. The initial conditions are specified by a Pierson–Moskovitz-type surface wave spectrum

$$S_s(k) = A\left(\frac{k}{k_p}\right)^{-3} \exp\left[-\frac{5}{4}\left(\frac{k}{k_p}\right)^{-2}\right], \quad k > 0;$$
$$S_s(k) = 0, \quad k \le 0, \tag{9}$$

with peak wavenumber k_p and a constant A that determines the significant wave height H_s (Pierson and Moskowitz 1964). These parameters also determine the average steepness of the initial spectrum $ak_s = \sqrt{2}\sigma_\eta k_p$, where σ_η is the standard deviation of the surface elevation (Tanaka and Wakayama 2015). The average steepness is the product of an average amplitude a and average wavenumber k_s, which, however, will only be used in their combination ak_s. For linear waves, the amplitude a is half the trough-to-crest wave height H, and this definition of the average steepness corresponds to the ratio of the significant wave height H_s and the dominant wavelength λ_p scaled by a factor $\sqrt{2}$. Generally, increased values of k_p and or A result in overall greater wave steepness, and thus increased nonlinearities.

The interface is initially undisturbed:

$$S_i(k) = 0, \quad -\infty < k < \infty. \tag{10}$$

The initial surface elevation $\eta_u(x, 0)$ and velocity potential Φ_u^S are synthesized from the initial spectrum at N_k evenly spaced wavenumbers k_j, $-20k_p < k_j < 20k_p$, with random, uniformly distributed phases. The wavenumber limit was chosen to be large compared to the critical wavenumber ($k_{\text{crit}} = 8.3$ for $R = 0.97$), but small enough not to severely limit the wavenumber resolution. The integration time step is $\Delta t = T_p/100$, where T_p is the period of the surface wave corresponding to k_p, and the evolution is calculated up to $t = 1500T_p$. We are specifically interested in the effect of class 3 triads, and therefore the order of the HOS is set to $M = 2$, which excludes the well-known four-wave interactions. Including four-wave interactions would add a slow evolution of the surface wave field and an additional downshift of the spectral peak, which could not easily be separated from the effects of the triad interactions.

3. Spectral evolution

As a test of the numerical code we reproduce some key findings of Tanaka and Wakayama (2015). We assume a deep lower layer for which $h_l = \infty$ and the critical wavenumber $k_{\text{crit}} = [4(1 - R)]^{-1}$. At low-density ratios this value can be close to the peak wavenumber k_p of realistic initial spectra (9), and a large fraction of the surface waves can be part of triads (Fig. 1), resulting in substantial changes of the spectral shape. For our test case with $R = 0.9$, $k_{\text{crit}} = 2.5$. Figure 2 shows the spectral evolution for $k_p = 2.0$, $A = 4 \times 10^{-4}$ ($ak_s = 0.050$) and $k_p = 4.0$, $A = 1.0 \times 10^{-4}$ ($ak_s = 0.071$). We normalize all spectral densities with the maximum value of the initial surface spectrum P_0. If $k_p < k_{\text{crit}}$ energy accumulates at k_{crit}, where a new peak forms, and spectral levels drop at high wavenumbers (Fig. 2a). On the other hand, for $k_p > k_{\text{crit}}$ the peak of the surface wave spectrum narrows and downshifts to k_{crit} (Fig. 2c). In both cases the new peak development takes <100 wave periods, and long interfacial waves with $k_i \ll k_{\text{crit}}$ develop, such that maximum spectral energy levels of the interfacial wave field can reach $O(10\%)$ of the peak surface wave energy levels (Figs. 2b,d). These spectral changes are qualitatively consistent with those for $R = 0.8$ discussed by Tanaka and Wakayama (2015). Their simulations did not include wave breaking, and the qualitative agreement with their results provides evidence that our parameterization does not affect the spectral modifications by triads when wave breaking is not substantial. Most importantly, our results confirm that in a two-layer fluid triad interactions can generate a spectrum of interfacial waves and substantially alter the initial surface wave spectrum. However, such strong density differences, $\rho_u = 0.9\rho_l$, do not exist in the oceans or natural lakes.

Increasing the density ratio ($R \to 1$) implies an increase in k_{crit}, and therefore limits the possible triad interactions to the high wavenumber tail of the surface spectrum (Fig. 1). Density differences in the ocean are typically very small, with $R > 0.99$ in open ocean surface mixed layers. As a limiting case for realistic oceanic densities we use $R = 0.97$ which corresponds to a salinity stratified two-layer fluid of freshwater overlying saltwater with salinity ≈30 psu, corresponding to, e.g., strongly stratified estuaries or regions of freshly melted sea ice. Slightly lower R values could be achieved if temperature differences are considered in addition to the salinity stratification.

In the following we perform a series of two-layer flow simulations with fixed density ratio $R = 0.97$, and fixed layer depth $h_u = 1$, $h_l = 200$ but varying initial surface wave fields, specified by the peak wavenumber k_p and the constant A [Eq. (9)]. Even for this weak density ratio, class-3 triads can result in substantial modification of the surface wave spectrum (Figs. 3a,c). With the normalization $g = 1$, and the integral of the elevation spectrum directly represents the energy per unit mass. If $k_p \ll k_{\text{crit}}$, (as illustrated for $k_p = 4.0$, $A = 2 \times 10^{-4}$, $ak_s = 0.10$) the peak of the spectrum becomes more pronounced and there is moderate loss of energy (per unit mass) at all wavenumbers $k_s > k_p$. If $k_p \approx k_{\text{crit}}$ ($k_p = 9.0$, $A = 0.5 \times 10^{-4}$, $ak_s = 0.17$) there is large energy loss (per unit mass) for $k_s > k_p$, large energy gain (per unit mass) at $k_s < k_p$, and a downshift of the peak. The density ratio also has a strong effect on the generation of the interfacial wave field. For $R = 0.97$ the relative energy gain (per unit mass) of the interfacial wave field is generally much less than in the case of $R = 0.90$ (Figs. 3b,d).

Thus, the triad interactions affect the spectral properties of the surface spectra in two main ways: (i) downshift of the peak

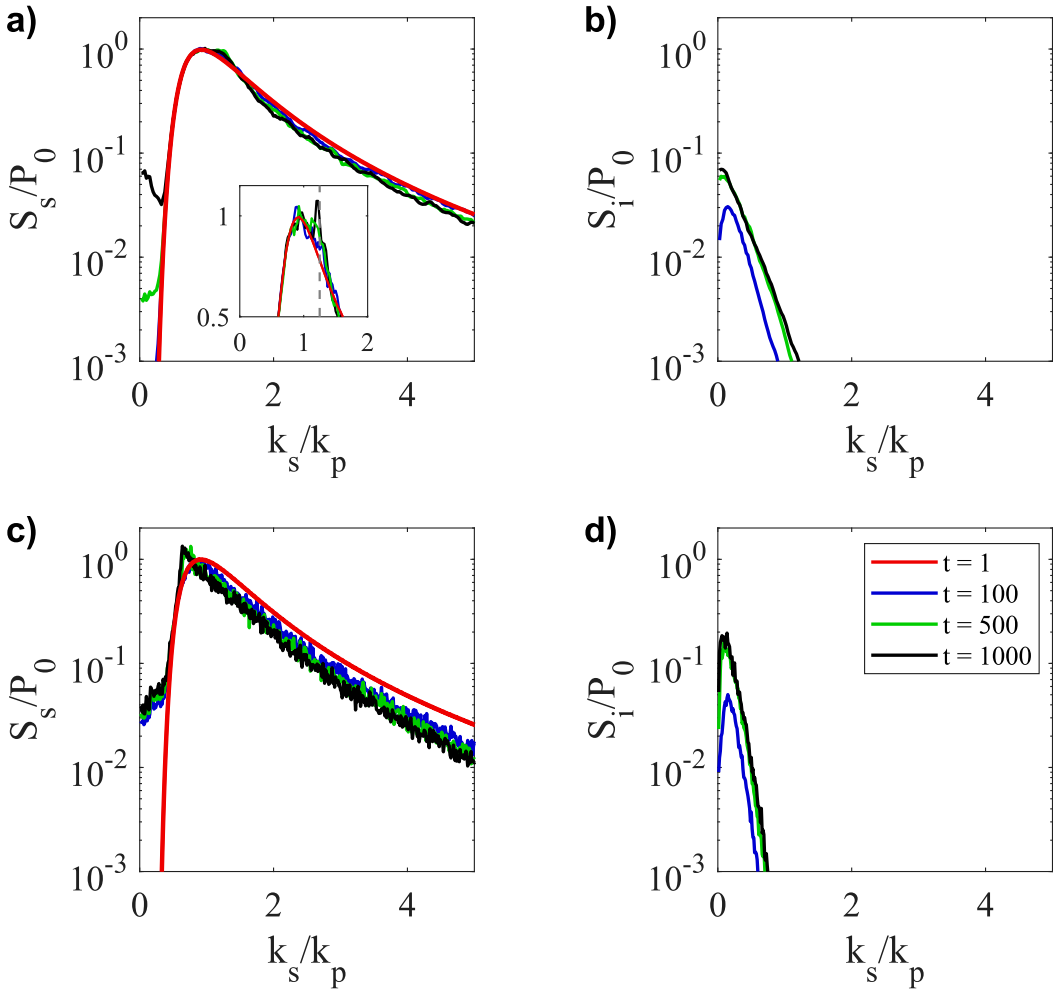

FIG. 2. (a),(c) Evolution of normalized surface wave spectra and (b),(d) interfacial wave spectra for $R = 0.90$. Spectral power is scaled by the maximum value P_0 of the initial surface wave spectrum. Time t is normalized by the peak period of the surface waves T_p. The vertical dashed line indicates $k_{\text{crit}} = 2.5$. (top) $k_{\text{crit}} > k_p$, ($A = 4 \times 10^{-4}$, $k_p = 2$). (bottom) $k_{\text{crit}} < k_p$, ($A = 1.0 \times 10^{-4}$, $k_p = 4$). The insert in (a) shows the spectral peak region on a linear scale.

and (ii) overall energy loss. Both depend on the peak wavenumber k_p and the amplitude A, and thus the average steepness of the initial spectrum ak_s.

We map out the modifications for peak wavenumbers $1 \leq k_p \leq 9.0$ and amplitude parameters $0.5 \times 10^{-4} \leq A \leq 8 \times 10^{-4}$, but restrict the model runs to cases with $ak_s \leq 0.2$. Simulations with greater steepness imply a large fraction of the initial surface waves having individual steepness at or above the breaking limit which would immediately be adjusted, and does not represent physically meaningful initial conditions.

The spectral peak downshift $\Delta k_p = k_p(t = 0) - k_p(t = 1500)$ is illustrated in Fig. 4. Most initial spectra with $k_p > 4.0$ experience a downshift, such that the shift increases with increasing steepness and increasing proximity of k_p and k_{crit}. For $4.0 < k_p \ll k_{\text{crit}}$ the downshift is $\Delta k_p \approx 1$. The strongest downshift, $\Delta k_p \approx 2$, occurs for the steepest initial wave fields. Weak upshift, $\Delta k_p < 0$ is found for some cases with $k_p \ll k_{\text{crit}}$. Figure 4 shows that for reasonably steep initial waves the peak waves can be affected even if the critical wavenumber lies in the high wavenumber tail of the initial spectrum.

Next, we consider the change in the total wave energy (per unit volume) relative to the energy of the initial surface wave field

$$\Gamma_s = \frac{\rho_u \left[\int_0^{20k_p} S_s(k, t = 0)\, dk - \int_0^{20k_p} S_s(k, t = 1500)\, dk \right]}{\rho_u \int_0^{20k_p} S_s(k, t = 0)\, dk}, \quad (11)$$

and

$$\Gamma_i = -\frac{(\rho_l - \rho_u) \left[\int_0^{20k_p} S_i(k, t = 0)\, dk - \int_0^{20k_p} S_i(k, t = 1500)\, dk \right]}{\rho_u \int_0^{20k_p} S_s(k, t = 0)\, dk}, \quad (12)$$

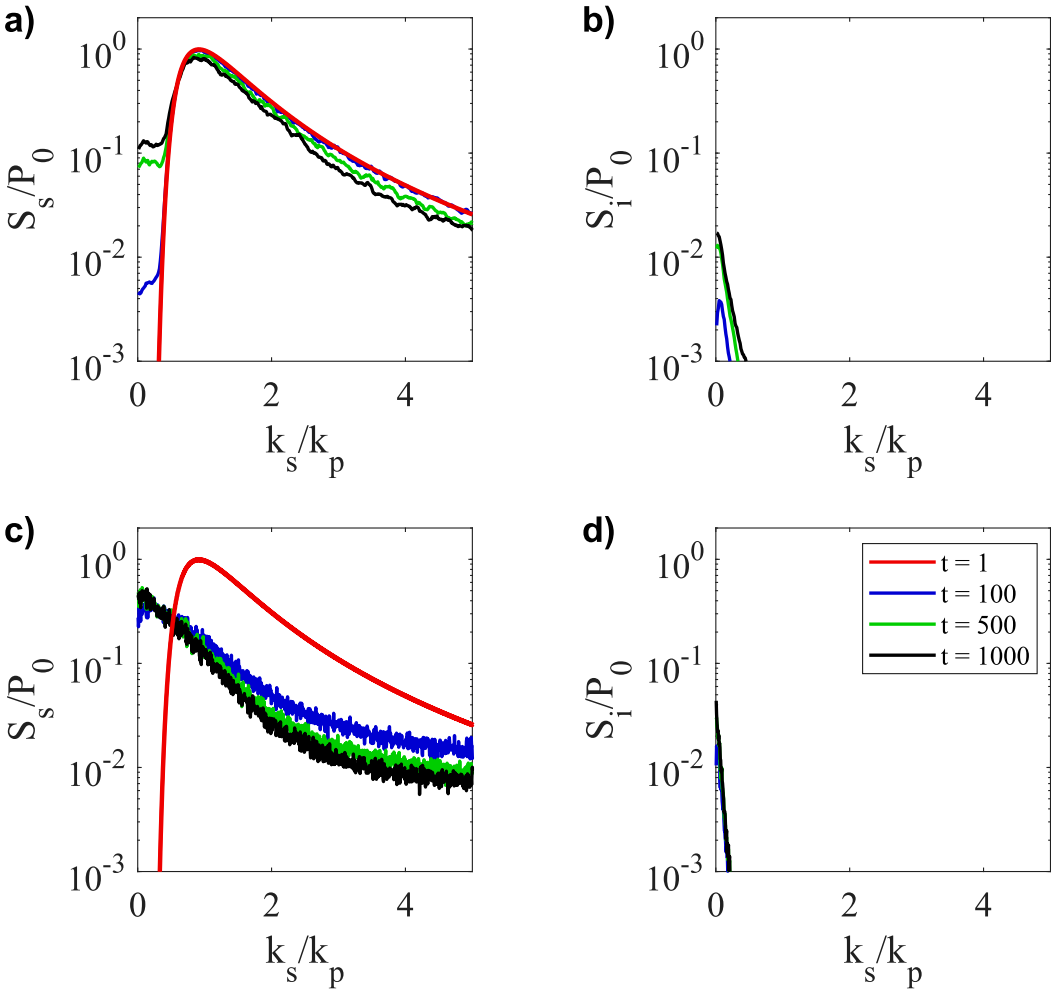

FIG. 3. As in Fig. 2, but for $R = 0.97$ ($k_{crit} = 8.7$). (a),(b) $k_{crit} \gg k_p$, ($A = 1 \times 10^{-4}$, $k_p = 4$). (c),(d) $k_{crit} \approx k_p$, ($A = 0.5 \times 10^{-4}$, $k_p = 9$).

for the surface and the interfacial wave field, respectively.

For $R = 0.97$ and small peak wavenumbers, $k_p < 2.5$, the surface wave field does not experience any noticeable energy loss (Fig. 5a). Above that threshold, energy loss increases monotonically with increasing peak wavenumber and with increasing spectral density parameter A, with Γ_s reaching up to 0.5. A small fraction of the energy loss of the surface wave field is converted into energy of the interfacial waves, while the major part is dissipated. The partition is strongly sensitive to the parameter values. The strongest relative energy gain by interfacial waves $\Gamma_i \approx 1.8 \times 10^{-3}$ occurs at moderate peak wavenumbers, $4 \leq k_p \leq 6$ and small spectral density, $A \leq 3 \times 10^{-4}$ (Fig. 5b). In these regions of the k_p, A space the energy loss of the surface wave field is $\Gamma_s \lesssim 0.2$. For wave fields with the strongest surface wave energy loss, $\Gamma_s \gtrsim 0.2$, the relative interfacial wave gain is much less, $\Gamma_i \lesssim 1 \times 10^{-3}$. Interestingly, interfacial waves are generated for all combinations of k_p, A of the initial surface wave spectrum, even for $k_p \lll k_{crit}$.

The simulations were repeated for the same set of initial surface wave spectra, but with a prescribed initial interfacial wave spectrum. Interfacial wave spectra cannot have an arbitrary shape, and as a realistic choice we take the fully developed spectrum after 1500 wave periods ($t = 1500$) from the simulations discussed above as initial interfacial spectrum for a given set of [k_p, A]. The final results are indistinguishable from the runs with an initially undisturbed interface (not shown). The spectral levels of the interfacial wave fields are slightly enhanced for $t \lesssim 200$, only, without any noticeable difference in the surface wave spectra.

The spectral downshift (Fig. 4), and the surface wave energy loss (Fig. 5) both show a roughly monotonic increase with k_p and A, and thus an increase with increasing average steepness of the initial spectrum ak_s. The total energy loss of the surface wave field is well correlated with the wave steepness and shows a clear threshold behavior, with no noticeable energy loss for wave steepness $ak_s < 0.05$ (Fig. 6). For steeper waves energy loss increases rapidly. A secondary parameter is the separation of the spectral peak and the critical wavenumber, with energy loss for $k_p \ll k_{crit}$ having a larger energy loss at the same wave steepness. For a two-layer fluid the curve seems to

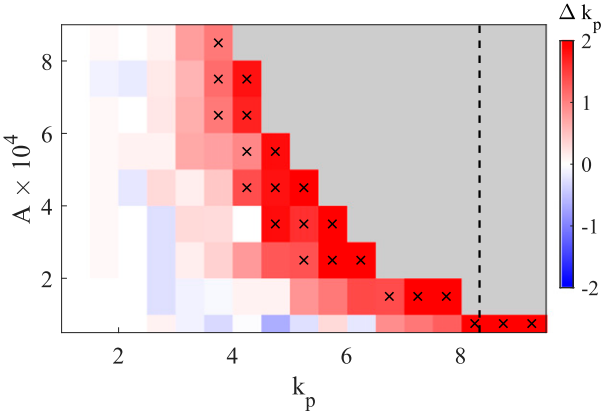

FIG. 4. Downshift of spectral peak of surface wave field after $1500T_p$, $R = 0.97$. The vertical dashed line indicates k_{crit}. Gray regions indicate $ak_s > 0.2$, and crosses indicate initial wave steepness $ak_s \geq 0.15$.

be weakly sensitive to the density ratio R, since the curve for $R = 0.90$ (Fig. 6a) and for $R = 0.97$ (Fig. 6b) are nearly identical. The median energy loss for $R = 0.90$ is about 2% greater than that for $R = 0.97$. The surface wave field on a homogeneous fluid ($R = 1.0$) is only subject to wave breaking and the median energy loss is 44% of that of $R = 0.97$ (Fig. 6c). Given

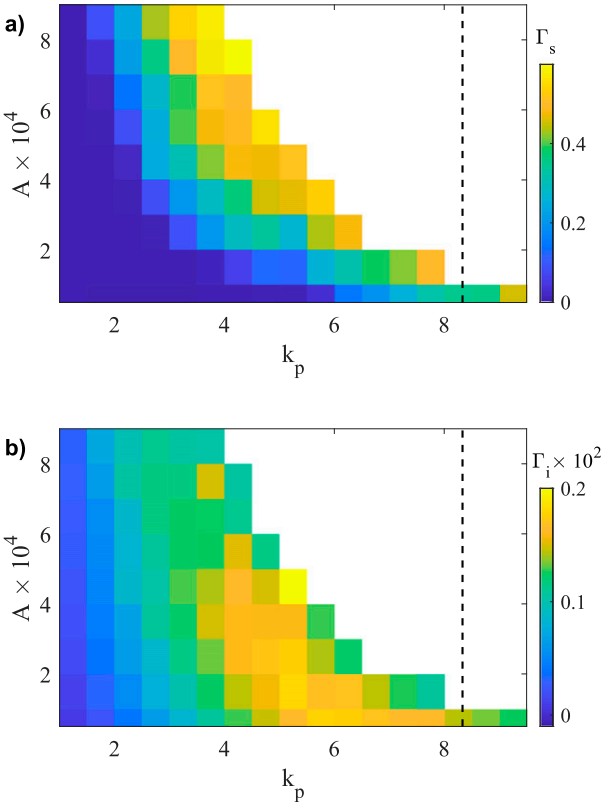

FIG. 5. Relative change of spectral energy after $1500T_p$ ($t = 1500$), $R = 0.97$. (a) Energy loss Γ_s of the surface wave field. (b) Energy gain Γ_i of the interfacial wave field.

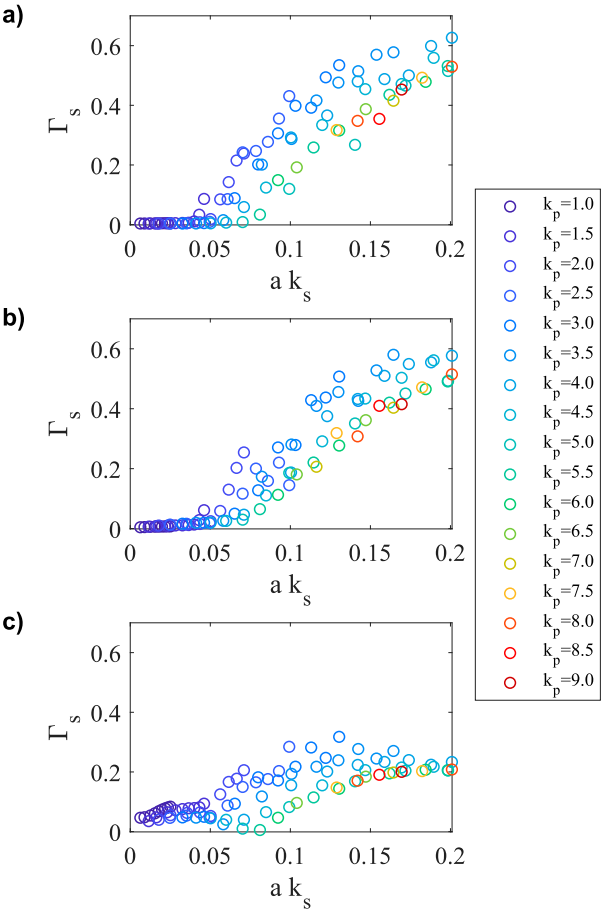

FIG. 6. Relative energy loss Γ_s of the surface wave field as function of steepness ak_s of the initial wave field. Color indicates the initial peak wavenumber k_p. (a) Density ratio $R = 0.90$. (b) Density ratio $R = 0.97$. (c) Homogeneous fluid ($R = 1.0$).

that only a small amount of energy is taken up by the interfacial waves, it is clear that dissipation of surface wave energy is clearly enhanced by the presence of the density interface and the coupling between surface and interfacial waves. This enhancement is a result of changes in the wave spectrum produced by coupling of the surface and interfacial wave fields.

In contrast to the total surface wave energy loss, the energy gain of the interfacial wave field Γ_i is not a function of only the initial surface wave steepness (Fig. 7). For low steepness, the gain increases with increasing steepness and reaches a maximum at $ak_s \approx 0.07$. However, the maximum value increases with the peak wavenumber. At greater steepness, Γ_i decreases, and for $R = 0.97$ it plateaus at about half the maximum value. The relative gain Γ_i is about 3–4 times greater for strong density ratios, $R = 0.9$ (Fig. 7a) compared to $R = 0.97$ (Fig. 7b).

The average steepness of the interfacial wave field is $ak_{pi} = \sqrt{2}\sigma_i k_{pi}$ with the wavenumber k_{pi} corresponding to the peak of the interfacial waves and the standard deviation of the interfacial elevation $\sigma_i = 4\sqrt{\int S_i(k, 1500)\, dk}$. The peak of the interfacial spectrum is at low wavenumbers $0.05 \lesssim k_{pi} \lesssim 0.4$, yielding $ak_{pi} = O(10^{-4})$–$O(10^{-3})$.

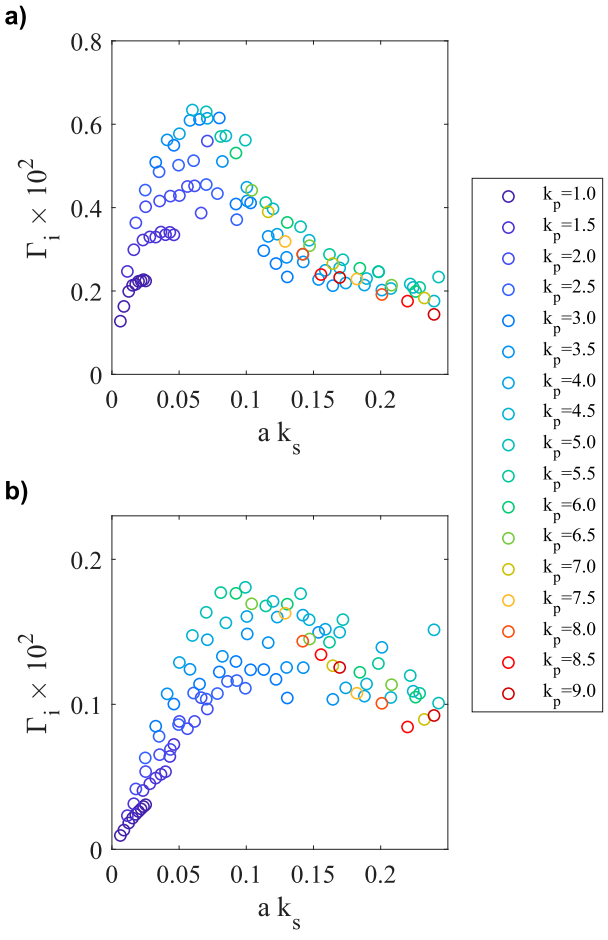

FIG. 7. Relative energy gain Γ_i of the interfacial wave field as function of steepness ak_s of the initial wave field. Color indicates the initial peak wavenumber k_p. (a) Density ratio $R = 0.90$. (b) Density ratio $R = 0.97$.

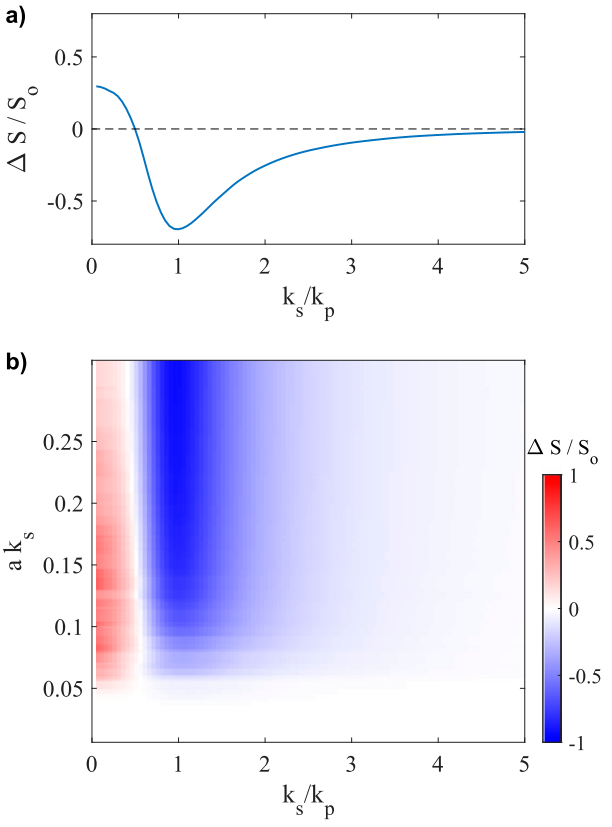

FIG. 8. Relative change of the surface wave spectral energy $\Delta S/S_o$ for $R = 0.97$. (a) Example with $k_p = 2.0$; $A = 3.0 \times 10^{-4}$. (b) As function of wave steepness ak_s, for all model runs.

The energy loss Γ_s of the surface waves is an approximately unique function of wave steepness, weakly dependent on density ratio or peak wavenumber. The energy transfer to the interfacial wave Γ_i on the other hand strongly depends on these parameters. The dissipation E_{diss} of surface wave energy is the difference between the total energy loss and energy transferred to the interface:

$$E_{\text{diss}} = (\Gamma_s - \Gamma_i)\,\rho_u \int S_s(k,0)\,dk. \tag{13}$$

For $R = 0.90$ about 98% of the surface energy loss is dissipated, and for $R = 0.97$ the fraction reaches 99.5%. Compared to surface waves, it takes very little energy to generate interfacial waves along a weak density gradient, which is reflected by the small fraction of surface energy used for the generation of the interfacial wave field.

The energy loss of the surface waves is not uniform across all wavenumbers, as can be seen in the evolution of the spectral shape (Fig. 3). In fact, there are wavenumber regions with energy gain, and others with energy loss. The relative spectral change $\Delta S/S_0$ can be treated as a spectral source function (Fig. 8), where $\Delta S = S_s(k, t = 1500) - S_s(k, t = 0)$, and $S_0 = \max[S_s(k, t = 0)]$. At the low end of the wavenumber range there is a net energy gain, and for $k \gtrsim 0.7k_p$ the spectral change is negative, with the strongest change happening at wavenumbers slightly greater than the peak wavenumber (Fig. 8a). This general shape of the source function holds for moderate to steep initial wave fields, $ak_s \gtrsim 0.06$ (Fig. 8b) and the region of negative change slightly expands with increasing wave steepness. In all cases, the spectral range of energy gain is smaller than that of the energy loss, and the maximum positive value is less than a third of the maximum negative value. Thus, the integral over the entire source function is always negative, consistent with $\Gamma_s > 0$ (Fig. 6).

4. Conclusions

In situations with strong upper-ocean stratification that can be approximated as a two-layer fluid, the surface wave field can undergo significant spectral evolution due to the stratification. The spectral change results in a net dissipation of surface wave energy, generation of interfacial waves, and a distinctive downshift of the spectral peak. This broad spectral response is surprising since these results are based on a HOS model which allows for wave triad interactions but excludes the

near-resonant four-wave interactions. Triad interactions are not possible in homogeneous deep water, and class-3 triad interactions which have been shown to exist in a two-layer fluid are restricted to wavenumbers $k_s > k_{crit}$. The spectral changes are a function of the characteristic steepness of the initial wave field, and do not directly depend on the position of the critical wavenumber within the spectrum. This result is striking and deserving of future study.

Our simulations are based on unidirectional wave fields on a two-layer fluid. While this simplification might be applicable to estuaries in fjords or narrow straits, in other applications like waves in the Arctic the analysis should be extended to a broad directional wave field. The growth rates of off-direction triad interactions are expected to be much smaller than that of aligned surface and interfacial waves (Zaleski et al. 2020). As a first approximation, neglecting off-direction triads, the modifications of a directional spectrum can be generated as a superposition of several 1D spectra undergoing colinear triad interactions.

The relative energy gain of the interfacial wave field Γ_i depends on the initial surface wave steepness ak_s and the generation of the interfacial wave field is most efficient for intermediate wave steepness $0.05 \lesssim ak_s \lesssim 0.09$. The lower value is also the threshold for the rapid increase in total energy loss of the surface wave field. This steepness threshold corresponds to the Pierson–Moskowitz spectrum of a fully developed wave field. The average steepness of developing wave fields is generally higher, and in a two-layer system this would result in increased energy dissipation. Nevertheless, long interfacial waves are generated in all cases. This energy is trapped to the interface, and as the waves steepen they can contribute to additional mixing between the two layers.

The main focus of this study is the modifications of the surface wave field, and the detailed study of the interfacial wave should be addressed in a future study. In particular, the development of instabilities and the interaction of interfacial waves with shoaling topography might be relevant to oceanic two-layer situations in fjords and the Arctic, as the waves approach the sloping coastal topography. Internal waves propagating onto a shoaling shelf have been observed (Klymak and Moum 2003) and modeled (e.g., Gemmrich and Klymak 2015) to be a source of enhanced turbulence and cause rapid temperature and velocity changes (Gemmrich and van Haren 2001). With an underlying velocity shear internal waves can develop Kelvin–Helmholtz instabilities as demonstrated in laboratory experiments (Troy and Koseff 2005) and observed in the deep ocean (van Haren and Gostiaux 2010).

Mixing due to surface wave generated turbulence has been observed to delay the freeze-up in the western Arctic (Smith et al. 2018). Mixing due to interfacial waves could have a similar effect but needs to be evaluated. Furthermore, the increased wave breaking at short wave lengths will increase near-surface turbulence (Gemmrich 2010), which is associated with increased air–sea gas exchange (Brumer et al. 2017).

In the real ocean, in contrast to our model study, four-wave interactions are not excluded and the narrowing of the spectral peak implies an increase in the Benjamin–Feir index (BFI; Janssen 2003), which could lead to a more pronounced wave group structure and a non-Gaussian surface elevation (Thomson et al. 2019). In the Arctic, the spectral downshift implies that wave energy can propagate further into the ice, since wave attenuation in ice decreases with wavelength (Collins et al. 2017). Thus, it is expected that the change of the spectral shape of the surface waves can affect ice break-up and refreezing.

The spectral modifications we find could be expressed as an additional source term in spectral wave models. Coupling such a modified wave model to ocean models will provide the required information on density gradients and upper-layer thickness, allowing the evaluation of additional mixing associated with the interfacial waves, and the altered evolution of the surface wave field.

Acknowledgments. The authors thank Prof. M. Tanaka (Gifu University) for providing the initial HOS code, and two anonymous reviewers for their comments. Funding for this project was provided by the Marine Environmental Observation, Prediction and Response (MEOPAR) network's Modelling Core. The computations were performed on WestGrid/Compute Canada (www.computecanada.ca). JG acknowledges support by the Institute for Baltic Sea Research (IOW) throughout his stay as a visiting scientist, and the many discussion that helped to shape the numerical simulations. AM acknowledges support from the Discovery Grant Program of the Natural Sciences and Engineering Research Council of Canada (funding reference RGPIN-2019-04986).

REFERENCES

Alam, M.-R., 2012: A new triad resonance between co-propagating surface and interfacial waves. *J. Fluid Mech.*, **691**, 267–278, https://doi.org/10.1017/jfm.2011.473.

——, Y. Liu, and D. K. P. Yue, 2009: Bragg resonance of waves in a two-layer fluid propagating over bottom ripples. Part II. Numerical simulation. *J. Fluid Mech.*, **624**, 225–253, https://doi.org/10.1017/S002211200800548X.

Ball, F., 1964: Energy transfer between external and internal gravity waves. *J. Fluid Mech.*, **19**, 465–478, https://doi.org/10.1017/S0022112064001550.

Banner, M. L., J. R. Gemmrich, and D. M. Farmer, 2002: Multiscale measurements of ocean wave breaking probability. *J. Phys. Oceanogr.*, **32**, 3364–3375, https://doi.org/10.1175/1520-0485(2002)032<3364:MMOOWB>2.0.CO;2.

Brodtkorb, P., P. Johannesson, G. Lindgren, I. Rychlik, J. Rydén, and E. Sjö, 2000: WAFO - a Matlab toolbox for the analysis of random waves and loads. *Proc. 10th Int. Offshore and Polar Eng. Conf.*, Vol. 3, Seattle, WA, ISOPE, 343–350.

Brumer, S. E., C. J. Zappa, B. Blomquist, C. W. Fairall, A. Cifuentes-Lorenzen, J. B. Edson, J. Brooks, and B. J. Huebert, 2017: Wave-related Reynolds number parameterizations of CO_2 *Geophys. Res. Lett.*, **44**, 9865–9875, https://doi.org/10.1002/2017GL074979.

Cavaleri, L., and Coauthors, 2018: Wave modelling in coastal and inner seas. *Prog. Oceanogr.*, **167**, 164–233, https://doi.org/10.1016/j.pocean.2018.03.010.

Collins, C. O., W. E. Rogers, and B. Lund, 2017: An investigation into the dispersion of ocean surface waves in sea ice. *Ocean Dynamics*, **67**, 263–280, https://doi.org/10.1007/s10236-016-1021-4.

Dommermuth, D. G., and D. K. P. Yue, 1987: A high-order spectral method for the study of nonlinear gravity waves. *J. Fluid Mech.*, **184**, 267–288, https://doi.org/10.1017/S002211208700288X.

Dysthe, K., H. E. Krogstad, and P. Müller, 2008: Oceanic rogue waves. *Annu. Rev. Fluid Mech.*, **40**, 287–310, https://doi.org/10.1146/annurev.fluid.40.111406.102203.

Ekman, V. W., 1904: On dead water. *Scientific Results of the Norwegian North Polar Expedition 1893–1896*, Vol. 5, F. Nansen, Ed., Longmans, Green and Co., 83–278 pp.

Gemmrich, J., 2010: Strong turbulence in the wave crest region. *J. Phys. Oceanogr.*, **40**, 583–595, https://doi.org/10.1175/2009JPO4179.1.

——, and H. van Haren, 2001: Thermal fronts generated by internal waves propagating obliquely along the continental slope. *J. Phys. Oceanogr.*, **31**, 649–655, https://doi.org/10.1175/1520-0485(2001)031<0649:TFGBIW>2.0.CO;2.

——, and C. Garrett, 2008: Unexpected waves. *J. Phys. Oceanogr.*, **38**, 2330–2336, https://doi.org/10.1175/2008JPO3960.1.

——, and ——, 2011: Dynamical and statistical explanations of observed occurrence rates of rogue waves. *Nat. Hazards Earth Syst. Sci.*, **11**, 1437–1446, https://doi.org/10.5194/nhess-11-1437-2011.

——, and J. M. Klymak, 2015: Dissipation of internal wave energy generated on a critical slope. *J. Phys. Oceanogr.*, **45**, 2221–2238, https://doi.org/10.1175/JPO-D-14-0236.1.

Janssen, P. A. E. M., 2003: Nonlinear four-wave interactions and freak waves. *J. Phys. Oceanogr.*, **33**, 863–884, https://doi.org/10.1175/1520-0485(2003)33<863:NFIAFW>2.0.CO;2.

Klymak, J. M., and J. N. Moum, 2003: Internal solitary waves of elevation advancing on a shoaling shelf. *Geophys. Res. Lett.*, **30**, 2003GL017706, https://doi.org/10.1029/2003GL017706.

Lamb, H., 1932: *Hydrodynamics*. 6th ed. Dover Publication, 732 pp.

Ma, Y.-C., 1983: A study of resonant interactions between internal and surface waves based on a two layer fluid model. *Wave Motion*, **5**, 145–155, https://doi.org/10.1016/0165-2125(83)90031-8.

Olbers, D., and C. Eden, 2016: Revisiting the generation of internal waves by resonant interaction with surface waves. *J. Phys. Oceanogr.*, **46**, 2335–2350, https://doi.org/10.1175/JPO-D-15-0064.1.

Phillips, O., 1960: On the dynamics of unsteady gravity waves of finite amplitude. Part I. The elementary interactions. *J. Fluid Mech.*, **9**, 193–217, https://doi.org/10.1017/S0022112060001043.

Pierson, W. J., and L. Moskowitz, 1964: A proposed spectral form for fully developed wind seas based on the similarity theory of S. A. Kitaigorodskii. *J. Geophys. Res.*, **69**, 5181–5190, https://doi.org/10.1029/JZ069i024p05181.

Smith, M., and Coauthors, 2018: Episodic reversal of autumn ice advance caused by release of ocean heat in the Beaufort Sea. *J. Geophys. Res. Oceans*, **123**, 3164–3185, https://doi.org/10.1002/2018JC013764.

Stokes, G. G., 1880: Supplement to a paper on the theory of oscillatory waves. *Mathematical and Physical Papers*, Cambridge University Press, 314–326.

Tanaka, M., and K. Wakayama, 2015: A numerical study on the energy transfer from surface waves to interfacial waves in a two-layer fluid system. *J. Fluid Mech.*, **763**, 202–217, https://doi.org/10.1017/jfm.2014.668.

Thomson, J., J. Gemmrich, W. E. Rogers, C. O. Collins, and F. Ardhuin, 2019: Wave groups observed in pancake sea ice. *J. Geophys. Res. Oceans*, **124**, 7400–7411, https://doi.org/10.1029/2019JC015354.

Thorpe, S., 1966: On wave interactions in a stratified fluid. *J. Fluid Mech.*, **24**, 737–751, https://doi.org/10.1017/S002211206600096X.

Troy, C., and J. R. Koseff, 2005: The instability and breaking of long internal waves. *J. Fluid Mech.*, **543**, 107–136, https://doi.org/10.1017/S0022112005006798.

van Haren, H., and L. Gostiaux, 2010: A deep-ocean Kelvin-Helmholtz billow train. *Geophys. Res. Lett.*, **37**, L03605, https://doi.org/10.1029/2009GL041890.

WAVEWATCH III Development Group, 2016: User manual and system documentation of WAVEWATCH III version 5.16. NOAA/NWS/NCEP/MMAB Tech. Note 329, 326 pp., https://polar.ncep.noaa.gov/waves/wavewatch/manual.v5.16.pdf.

Zaleski, J., P. Zaleski, and Y. V. Lvov, 2020: Excitation of interfacial waves via surface-interfacial wave interactions. *J. Fluid Mech.*, **887**, A14, https://doi.org/10.1017/jfm.2019.1033.